Applied Surface Science 546 (2021) 149099

Contents lists available at ScienceDirect

Applied Surface Science

journal homepage: www.elsevier.com/locate/apsusc

Full Length Article

Tracking the chemical active species to unravel the photocatalytic activity evolution of structure modified polymeric carbon nitride

Ziyang Dai [a,b], Guangxing Zhao [a,b], Fangxing Ma [a], Wenhai Zhang [a], Yan Gong [a], Hongkun Li [a], Xiuming Zhang [a], Naibo Lin [a], Lei Liu [b], Da Zhan [a,b,*]

[a] College of Materials, Xiamen University, Xiamen, Fujian 361005, China
[b] State Key Laboratory of Luminescence and Applications, Changchun Institute of Optics, Fine Mechanics and Physics, Chinese Academy of Sciences, Changchun, Jilin, 130033, China

ARTICLE INFO

Keywords:
Active species
Photocatalytic degradation
Polymeric carbon nitride
Oxygen doping
Heterojunction

ABSTRACT

Herein, a series of structure modified polymeric carbon nitride (PCN) started from the same precursor were prepared by a step-by-step method. The photocatalysts show different catalytic performance in degradation of Rhodamine (RhB) and methyl orange (MO). The doping treatment endows photocatalysts improved activity for decomposing RhB molecules. Subsequently heterojunction formation by incorporation of Ag-related species facilitates the degradation of the MO molecules, but it seems like at the expense of the activity of RhB molecules decomposition. By combining studying the evolutions of micro-structure, electronic structure, and spatial charge separation of each sample, we found that the photoluminescence reflected spatial charge separation effect cannot be used to fully explain aforementioned trends of the photocatalytic activity. In this background, we systematically studied the roles of each individual active species that influenced photocatalytic performances for each sample, and a reasonable degradation mechanism on the basis of roles of different active species is proposed to interpret the above photocatalytic phenomena in detail. Furthermore, we believe that this work not only presents a facile route to modify catalyst for enhancing photocatalytic performance, but the more important is that, it reveals the enhancement mechanism from the viewpoints by combining both effective charge separation and proportion evolution of active species.

1. Introduction

Converting the infinite solar energy to accessible chemical energy form is the persevered objective for human being, and thus it has obtained intensively exploration in both scientific and industrial communities persistently [1,2]. Since Honda and Fujishima discovered the photocatalytic effect by using TiO_2 and Pt co-catalyst in 1972 [3], the unprecedented advances have been taken by modification of appropriate carriers to build efficient photocatalytic system [4]. Typically, among enormous inorganic semiconductor-based photocatalysts that possess suitable band gaps like metal oxides [5], metal sulfides [6], oxynitrides [7] and so forth, present good photocatalytic activity but simultaneously bring side effects that are not tolerant, such as toxicity and environmentally unfriendly issues [8]. In the recent decade, polymeric carbon nitride (PCN) as a photocatalyst material [9] has conducted a great tendency in the field of organic pollution degradation and water splitting for sunlight harvest utilization because of its metal-free, stable, wide visible light absorption band, low cost and facile synthesis [10]. Nevertheless, for pristine CN, relatively high recombination of light excited electron-hole pairs gives rise to the insufficient photocatalytic activity [11]. Recently, the introduction of surface defects [12,13] and synthesis of PCN-based heterojunction [14,15] have been widely applied for optimizing the performance. It can be clearly seen in table S1 that decorating PCN-based composites can enhance the photocatalytic performance [16], but the degradation mechanism of photocatalysis is still in debate [17,18]. For example, it is noted that even for degradation of the same dye, the active species rankings in photocatalysis changed irregularly by structure modifications. Specifically for RhB degradation by PCN-based composites, Feng and co-workers demonstrated that •OH and h^+ play the key role when employing P@PCN-15 as a photocatalyst [19]. Tan and co-workers reported that $\bullet O_2^-$ and h^+ are the main active species in the heterojunction of mpg-C_3N_4/$BiPO_4$ [20]. Jiang and co-workers found that using Ta_3N_5/g-C_3N_4 as a photocatalyst, h^+ and $^{\bullet}OH$ are the primarily contributive species

* Corresponding author at: College of Materials, Xiamen University, Xiamen, Fujian 361005, China.
E-mail addresses: zhanda@xmu.edu.cn, zhanda@ciomp.ac.cn (D. Zhan).

https://doi.org/10.1016/j.apsusc.2021.149099
Received 1 December 2020; Received in revised form 6 January 2021; Accepted 18 January 2021
Available online 20 January 2021

[21]. Furthermore, Shi and co-workers reported that the contribution of active species in organic pollutants degradation is varied with the change of light source wavelength from NIR light to visible light [22]. It can be obviously seen that the mechanism behind the enhanced photocatalytic performance cannot be interpreted by just a simple effective charge separation model [23–25]. Therefore, unraveling the role of active species and related mechanisms is of great importance for guiding more efficient researches in photocatalysis. In this work, as a prime photocatalytic activity concern, the active species evolution for RhB molecules degradation process is discussed in detail. Subsequently, the performance of the MO molecules degradation is a subsidiary indicator. On this basis, we have designed a 4-step route to finally obtain a perfect photocatalyst with improved performances, and acquired relatively systematic conclusion for the photocatalytic mechanism. The effective charge separation is extrinsic factors that influenced photocatalysts performance, and the reasonable proportion of active species is intrinsic factor for affecting photocatalytic degradation activity.

2. Experimental section

2.1. Synthesis of polymeric carbon nitride (PCN)

In this work, five types of PCN-based catalysts were fabricated for comparison as shown in Scheme 1. It can be seen that all the samples were derived from the same original precursor with structure modification step by step. Firstly, the polymeric carbon nitride bulk was synthesized in a typical procedure by melamine as initial precursor calcined in a quartz tube furnace [26]. Typically, 10 g melamine powder was uniformly dispersed in a covered Al_2O_3 crucible, subsequently heated at 550 °C for 4 h with ramping rate of 5 °C /min, obtaining polymeric carbon nitride bulk powder (denoted as PCN as shown in Scheme 1b and Fig. S1-i).

2.2. Synthesis of annealed samples

The PCN powder was put into crucible to anneal at 500 °C for 2 h (at a rate of 5 °C/min). The obtained sample was slightly deep yellow, which was collected as a new catalyst for the subsequent work (denoted as annealed-500 as shown in Scheme 1c and Fig. S1-ii).

The annealed-500 sample was reannealed again at 450 °C for 1 h with the ramping rate of 5 °C/min started from room temperature. The reannealed sample is the powder presented pure white color as can be seen in Scheme 1d and Fig. S1-iii, and it is denoted as reannealed-450 throughout the whole paper.

2.3. Preparation of heterojunction samples

The synthesis of Ag_2CO_3-CN (Scheme 1e and Fig. S1-iv) was through the following method: 0.1 g reannealed-450 was dispersed into 140 ml deionized water with 0.5 h stirring, then the suspension was sonicated for 1 h to make the reannealed-450 uniformly dispersed, subsequently, 4.35 ml $AgNO_3$ solution (0.05 mol/L) was added to suspension dropwise and stirred for another 1 h to enable Ag^+ uniformly adsorbed on the reannnealed-450 surface during a dark condition. The 5 ml $NaHCO_3$ solution (0.05 mol/L) was added into the mixture drop by drop with 2 h stirring. The final product was purified by centrifugation and washed with sufficient deionized water several times, then dried with the lyophilizer in vacuum for 24 h. The corresponding High loading Ag_2CO_3-CN used the same method obtained, which just improved the load of the Ag_2CO_3.

The Ag-CN heterojunction (Scheme 1f and Fig. S1-v) was prepared through the phase transformation synthesis, of which the Ag_2CO_3-CN synthesized at the previous step was put into an open crucible and calcined in air at 220 °C for 10 min (ramping rate 5 °C/min) in a quartz tube furnace, then taken it out immediately. The transformation from Ag_2CO_3 to Ag was confirmed by the XRD results, and it will be discussed in detail later.

2.4. Characterization

The quartz tube furnace (OTF-1200X) was employed to calcine products in air condition. The powder diffraction of x-rays was detected on a Bruker D8 Advance X-ray diffractometer with Cu Kα radiation. The morphology of the catalysts was captured by a field emission scanning electron microscope (SU-70, Hitachi). The transmission electron microscope images, EDX and elemental mapping were recorded by FEI Talos-F200s. Atomic force microscopy (AFM) image was operated by a Bruker Dimension FastScan. Fourier transform infrared spectra were conducted with a Nicolet-is10 of the Thermo Fisher Scientific. The XPS measurements were performed on K-Alpha of the Thermo Scientific. Atomic force microscopy test was operated by a Bruker Dimension FastScan. The nitrogen adsorption–desorption isotherms were acquired on Tristar 3020 (Micromeritics Instrument (shanghai) co., LTD). The UV–Vis adsorption spectra were gathered measured by a UV-1800

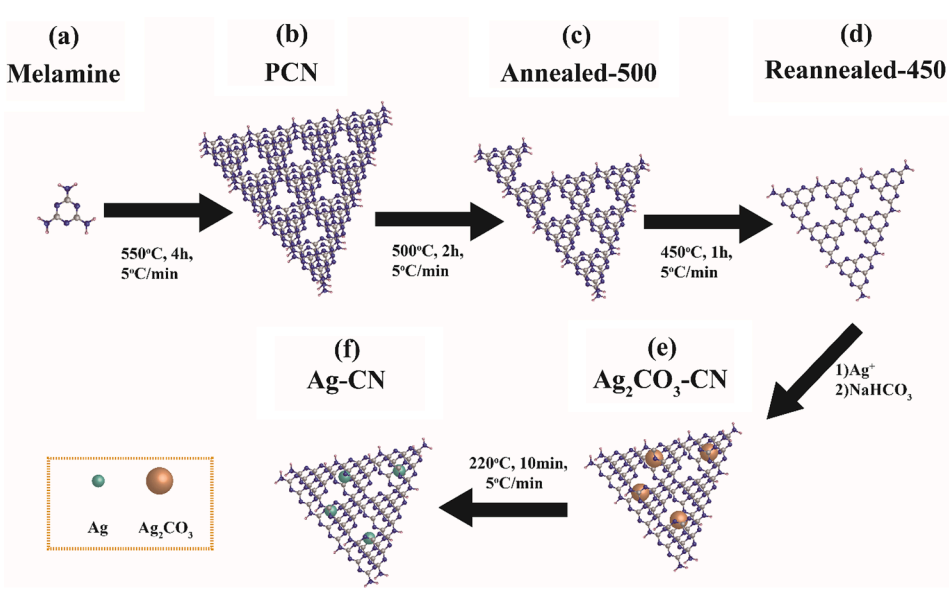

Scheme 1. Scheme illustration of the fabrication of PCN-based composites photocatalyst.

spectrophotometer. The photoluminescence (PL) measurements were recorded with a Horiba HR Evo system, and the excitation laser wavelength was 325 nm with × 40 UV lens.

2.5. Photocatalytic performance test

Rhodamine B and Methyl Orange molecules degradation measurements were evaluated to illuminate the photocatalytic activity in a closed Pyrex glass that was top-irradiation reactor using 300 W xenon lamp with a 400 nm cutoff filter. 15 mg catalysts were dispersed in 90 ml 5 ppm (or 10 ppm) RhB (or MO) solution. During a certain interval, 1 ml suspensions were taken out and centrifuged to get rid of the catalyst. The organic dye solution degradation evolution was recorded by UV–Vis spectrophotometer.

3. Results and discussion

3.1. Characterization of physical properties

The crystal structures of various CN-based composites were characterized by XRD (Fig. 1a). It can be obviously seen that two evident peaks appeared in the PCN sample, one is the strongest diffraction located at ~ 27.62° and the other is relatively weak peak at ~ 12.77°, corresponding to the characteristic interlayer stacking reflecting conjugated aromatic systems (0 0 2) and in-planar units packing of the tri-s-triazine (1 0 0) [27], respectively. After the annealing treatment, the strongest diffraction peak gradually shifts to a high angle degree at ~ 27.97°, indicating the shrink of the inter-plane distance [28]. Furthermore, it is noted that the full width of half maximum (FWHM) of the (0 0 2) peak decreases after annealing treatment, indicating the natural defects in PCN decreased, and it is worth noting that the defects degree does not show obvious increase even after mixing with Ag-species compound (according to the FWHM evolution). Meanwhile, the relatively weak peak at ~ 12.77° becomes less distinct, suggesting that the break of hydrogen bonds of interlayer framework and the decreasing PCN layers [29]. Despite the fact that it is barely to detect Ag relevant diffraction peaks in heterojunction samples (pink and green curves in Fig. 1a), the diffraction peaks of Ag_2CO_3 and Ag can be obviously observed by loading higher Ag-related compound (Fig. 1b) using the same preparation methods [30]. Therefore, the XRD result indicates that the phase transformation from Ag_2CO_3 to Ag was succeed, and Ag_2CO_3 and Ag were respectively loaded on PCN samples (Scheme 1e and f).

The morphology evolution of the modified samples was observed by SEM and TEM. It can be seen SEM images in Fig. S2 that the PCN is undergone a dramatic oxidation etching process from solid bulk to petty filmy sheets during the annealing treatment (Annealed-500 and Reannealed-450) [31]. However, it can be found that the relative thick bulk structure was rebuilt after Ag_2CO_3 incorporated into reannealed-450 (Ag_2CO_3-CN) and the structure of phase transformation sample (Ag-CN) is almost unchanged.

The reannealed-450 and heterojunction samples were also observed by HRTEM. As shown in Fig. S3, the result of reannealed-450 is similar to other works on oxygen etching treated CN [32]. Surprisingly, the distinct lattice fringe of CN can be observed clearly almost everywhere for both Ag_2CO_3-CN and Ag-CN (~0.326 nm) as observed in Fig. 2b-c and i-j, which can be assigned to (0 0 2) of CN [27]. This is in agreement with XRD results.

To further confirm the elemental composition, the high-angle annular dark field (Fig. 2a, h) and the corresponding elemental mapping images are employed in detail. As shown in Fig. 2d-g and k-n, the elemental mapping of C, N, O and Ag is unambiguous presented in the sample of Ag_2CO_3-CN and Ag-CN, confirming the uniform elemental distribution on the interface of the carrier.

Besides, the reannealed-450 present ultrathin thickness as scanned by atomic force microscopy (AFM) (Fig. 3a and b), of which many small flakes (from hundred nm to a few μm) with average thickness of approximately ~ 1 nm can be observed, corresponded to 1–2 C-N atomic layers [33,34]. The ultrathin flakes may be very useful for facilitating photocatalytic process through its surface active groups [35,36], and Ag_2CO_3-CN and Ag-CN are also benefited from this as they were synthesized using reannealed-450 as precursor.

The chemical species composition is especially important to contribute the overall photocatalytic performance, thus, the elaborate chemical structures were further investigated by the FTIR and XPS, respectively. As shown in Fig. 3c, several absorption bands (3000–3300 cm^{-1}, 1200–1600 cm^{-1} and 805 cm^{-1}) could be assigned to the N-H stretching vibrations, typical C-N heterocycles stretching mode and the breathing mode of triazine units [37], respectively. It is noted that in Fig. 3d, the annealed-500 and reannealed-450 have a weak signal detected at ~ 1084 cm^{-1}(the gray background region), implying the oxygen related groups were possibly introduced after annealing process [38]. Moreover, the FTIR spectra of heterojunction samples possessed similar absorption bands with the reannealed-450, which means that heterojunction samples did not fiercely change the stretching and bending vibration of the samples except that decreased intensity peaks between 1000 and 1350 cm^{-1}. These results suggested that oxygen element was smoothly doped into PCN by covalent bonds without breaking the primary structure.

To further determine the evolution information of chemical structure and oxidation state of the catalyst, the X-ray photoelectron spectroscopy (XPS) was employed. As shown in Fig. S4, all samples are composed of C, N and O elements, the heterojunction samples also contain Ag element, which is in agreement with the EDX test (Fig. S5). It can be seen in Fig. S6 and 7 that no obvious shifts in the binding energy of both C1s and N1s spectra after the annealing treatment or Ag-species loading process, disclosing that the core structure of CN melon units was relatively chemical inertness [39].

Moreover, it can be found in Fig. 4a that the high resolution O1s

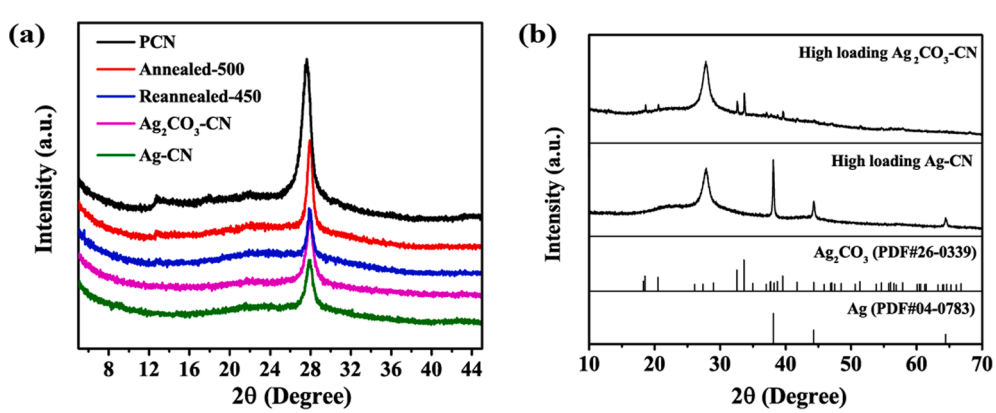

Fig. 1. (a) XRD patterns of the PCN-based samples and (b) the corresponding high loading heterojunction samples.

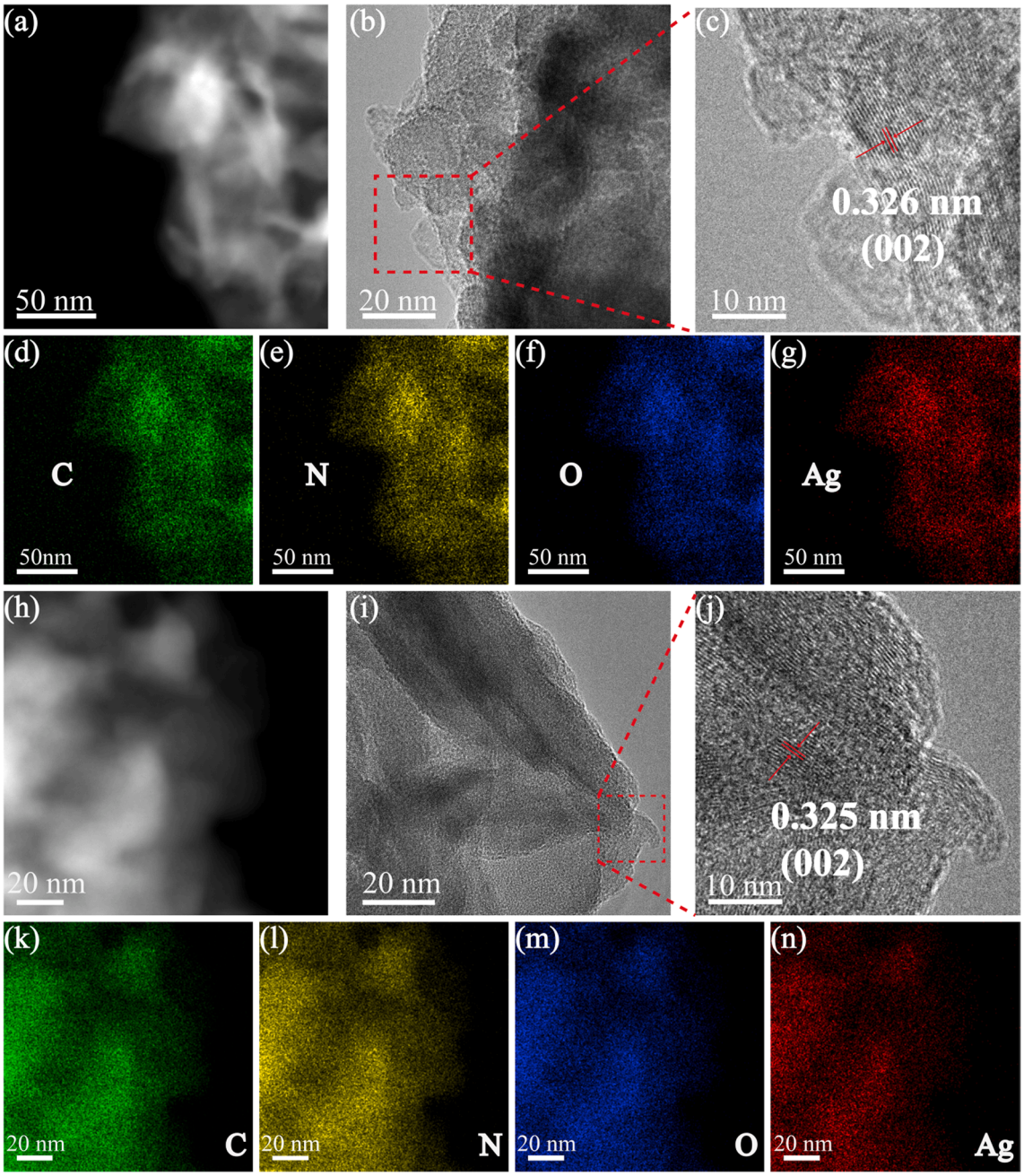

Fig. 2. (a) and (h) HAADF images, (b) and (i) low-magnification, (c) and (j) high-magnification. (d)-(g) and (k)-(n) the corresponding HRTEM elemental mapping of C, N, O, Ag of Ag_2CO_3-CN and Ag-CN, respectively.

spectrum of the PCN shows the core level at ~ 532.7 eV, ascribed to absorbed H_2O [22]. No additional signal related to the N-O or C-O bond can be observed for PCN. After annealing process, the other two core levels at ~ 534 eV and 531.6 eV are clearly detected on the annealed samples (Fig. 4b and c) [40]. These signals can be attributed to the formation of the absorbed O_2 and N-C-O species, respectively. Furthermore, it can be found that the peak (~531.6 eV) intensity of the reannealed-450 is stronger than that of annealed-500, indicating the increase of proportion of N-C-O bond. Interestingly, the new peak at ~ 531.2 eV emerged for Ag_2CO_3-CN shown in Fig. 4d after loading process [41], which can be ascribed to the oxygen in Ag_2CO_3. The Ag-CN is derived from pyrolysis of Ag_2CO_3, the phase transformation from Ag_2CO_3 to Ag causes vanished of the peak at ~ 531.2 eV (Fig. 4e). The evolution information of the catalyst is in agreement with XRD and FTIR results. Furthermore, the heterojunction samples had similar Ag spectra shown in Fig. 4f that had two individual peaks with the binding energies of 368.2 and 374.2 eV, which were assigned to Ag 3d5/2 and Ag 3d3/2, respectively [42].

The nitrogen adsorption–desorption isotherms of photocatalyst samples are shown in detail (Fig. 5a). In the relative pressure from 0.6 to 1.0, all of them disclosing typical type IV isotherms as H3 type hysteresis loops, indicating typical slit-formed mesoporous structure [43]. It can be seen in table S2 that the S_{BET} of PCN, annealed-500, reannealed-450, Ag_2CO_3-CN and Ag-CN is about 16.92, 152.75, 165.74, 74.29 and 74.30 $m_2\ g^{-1}$, respectively. It indicates that after sufficient annealing process, both annealed samples exhibited remarkable large surface areas with increasing pore volume. The decrease of surface area for the heterojunction samples can be ascribed to the loading of Ag-based compound on reannealed-450 to form aggregation-like structure. The corresponding pore size distribution plots (Fig. 5b) show an opposite evolution

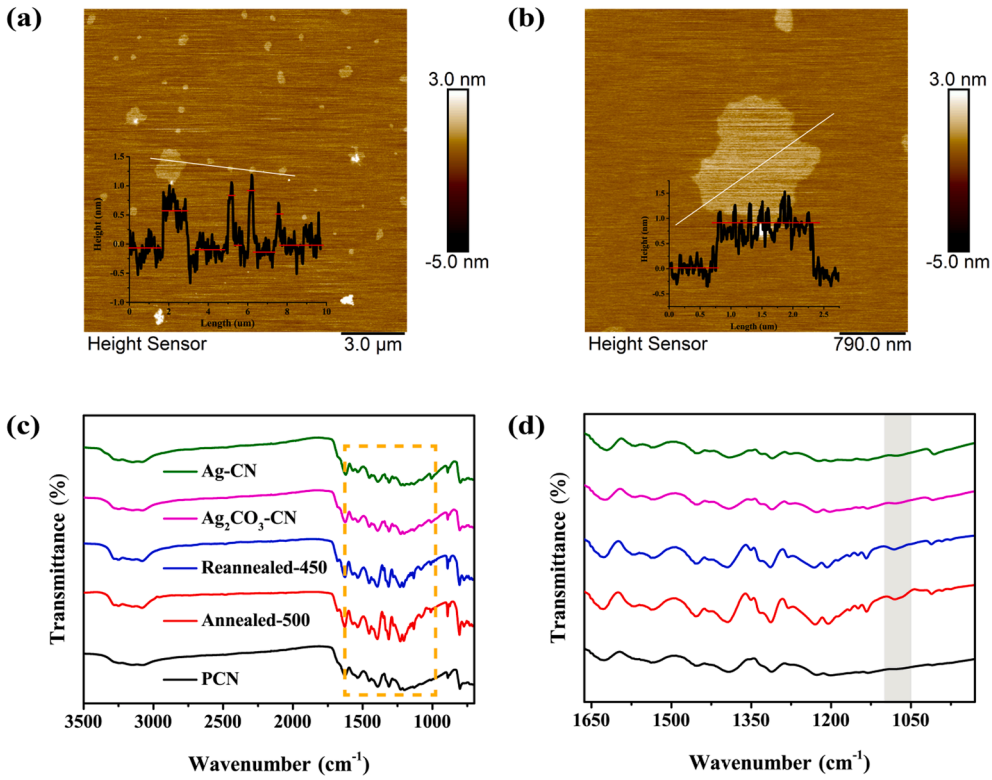

Fig. 3. (a) The AFM images of the reannealed-450 sample and (b) the corresponding enlarged image (The corresponding thickness curves determined along the white solid line, respectively). (c) FTIR spectra of PCN-based samples and the corresponding enlarged spectra (d) between 1000 and 1650 cm^{-1}.

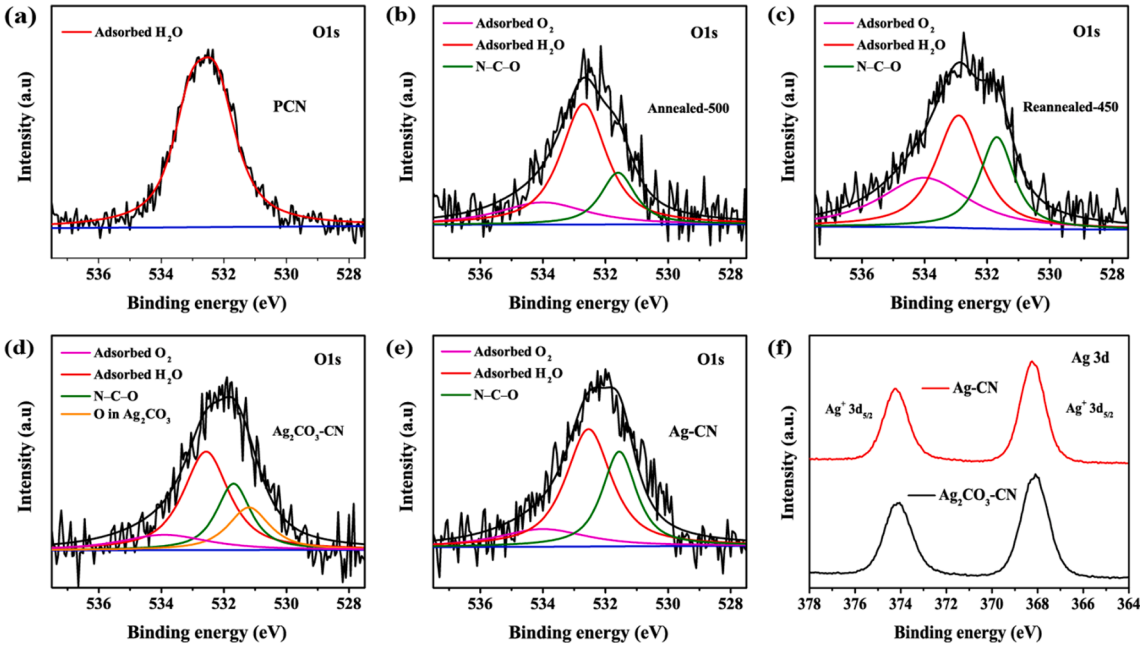

Fig. 4. High resolution XPS spectra of O1s for (a) PCN, (b) annealed-500, (c) reannealed-450, (d) Ag_2CO_3-CN and (e) Ag-CN, respectively. (f) High resolution XPS spectra of Ag 3d for the heterojunction samples.

trend compared to that of the BET result, and it further demonstrates the microstructure evolution.

3.2. Electronic properties

Furthermore, the evolution of internal electronic structure is also significant to give us new insights into what happened to photocatalytic activity. Since PCN is a well-known direct band gap semiconductor, the light can be efficiently absorbed when the energy of excitation photon is resonance for the band edge. As UV–vis absorption spectra can probe subtle difference of electronic structure of PCN, it can help us be aware of the evolution of modified electronic structure. It can be clearly shown in Fig. 5c that the light-harvesting ability of both annealed samples is reduced in the range from 400 to 550 nm (red and blue curves)

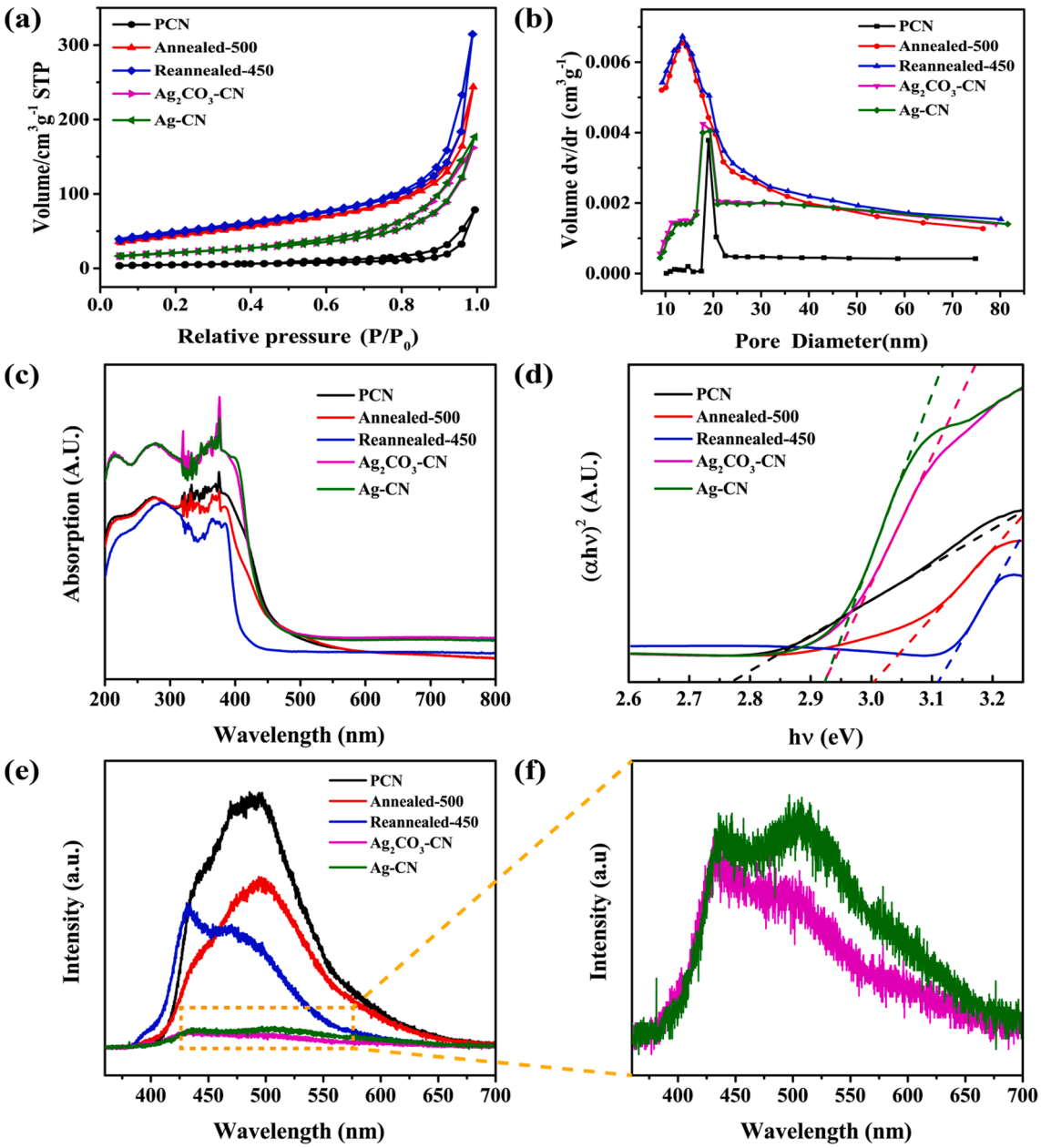

Fig. 5. (a) Nitrogen adsorption-desorption isotherms of PCN-based samples. (b) The corresponding pore size distribution plot. (c) The UV–Vis absorption spectra and (d) the corresponding derived optical band gaps spectra of PCN-based samples. (e) The PL spectra of PCN-based samples and (f) the corresponding enlarged PL spectra of heterojunction samples.

compared to that of the PCN (black curve), but the absorption of heterojunction samples is enhancement in visible light region [44] (purple and green curves). Using Kubelka–Munk theory, the light absorption spectra derived optical band gaps are evaluated. Fig. 5d directly reflects the evolution of the band gap with different treatments step by step. The annealed samples gradually shifted to high energy level from ~ 2.85 (PCN) to 3.05 (annealed-500) and 3.13 eV (reannealed-450), and the band gaps of both Ag_2CO_3-CN and Ag-CN shifted to ~ 2.95 eV.

In this work, the photoluminescence (PL) spectra of PCN-based samples were measured by monochromatic UV laser with 325 nm excitation wavelength. As shown in Fig. 5e, it can be found that PCN exhibits a strong PL signal located at ~ 470 nm and it blueshifts to ~ 430 nm during the sufficient annealing treatment (reannealed-450). Meanwhile, the peak of both heterojunction samples slightly redshifts to ~ 436 nm (Fig. 5f) when Ag-related species loading on reannealed-450. The evolution of the PL emission peak position is also in agreement with the trend of band gap shift. Furthermore, it is noted that the rate of recombination of excited electron-hole pair performs drastic decrease from annealing process to the metal loading treatment as reflected by the decreased PL intensity. This result indicates that oxygen doping assisted surface modification enables an effective recombination suppression of excited electron-hole pairs, and more importantly, forming heterojunctions are more efficient for photo-excited charge transfer for further suppressing electron-hole recombination, resulting more effective electron-hole separation.

3.3. Photocatalytic performance

With the suitable band gaps to effectively excite electron-hole pairs, PCN-based photocatalysts are able to generate H_2 though splitting water [45], bacteria disinfection [46], as well as degradation of organic pollutants [47]. The recent research shows that PCN may even be used as a

microwave absorbing material in the field of wireless communication and anti-radar detection [48]. In this work, the photocatalytic activity of samples is firstly elaborated by decomposing the RhB under visible light. As shown in Fig. 6a, the photocatalytic performance in degradation of RhB for annealed-500 and Ag_2CO_3-CN (red and green curves) is comparable, while the activity of reannealed-450 to that of Ag-CN (blue and orange curves) is comparable, and the latter two samples show much superior activities than that of the former two. Therefore, the macroscopic photocatalytic performance in degradation of RhB does not show the monotonous enhancement trend with chemical modification process, meaning that the photodegradation activity is not just as a simple function of structural modification process. Specifically, PCN performs relatively poor photocatalytic ability as only ~ 50% RhB were decomposed after 30 min. After annealing process, ~95% pollutant molecules were decomposed in 30 min using annealed-500 as the catalyst. The reannealed-450, manifests higher photo-degradation performance, would only take about 12 min to decompose the same RhB molecules (95%). Although the Ag_2CO_3-CN composite was derived from reannealed-450, photocatalytic activity (30 min, 95%) reduced by more than half compared with that of the reannealed-450 (12 min, 95%). However, by phase transformation treating of Ag_2CO_3-CN to form Ag-CN (Scheme 1f), the photocatalytic performance is dramatically improved to a level (15 min, 95%) almost comparable to that of the reannealed-450 (12 min, 95%). To evaluate the potential practicality photocatalysis, the renewability and stability measurements have been conducted. Ag-CN, as the typical photocatalyst prepared through 4 steps, still manifests good stability even after 4 successive RhB degradation cycles (Fig. 6b).

To further investigate the photocatalytic activity of samples, methyl orange (MO) is selected as another representative organic pollutant to evaluate photocatalytic performance. As shown in Fig. 6c, it is obviously seen that the Ag-CN ranked 1st out of five samples according to the performance in decomposing MO (90 min, 95%), much better compared to that of the reannealed-450 (90 min, 30%) though it performs best in decomposing RhB. It is also noted that for reannealed-450 (90 min, 30%), the performance in decomposing MO molecules is also much worse than that of Ag_2CO_3-CN (90 min, 85%, though it is not good for decomposing RhB). In other words, Ag_2CO_3-CN possesses higher proportion of radicals that facilitate the MO molecules decomposition, but such active radical species may be not effective to decompose the RhB molecules (Scheme 2, the detail will be discussed later). On the other hand, PCN and annealed-500 still performed very weak photocatalytic performance (90 min, ~12%) in decomposing MO molecules (The detailed degradation process reflected by the optical absorption spectra can be intuitively observed in Fig. S8). These results indicate that different pollutants can be effectively decomposed by selected suitable active species distribution.

Fig. 6d summarized the aforementioned photocatalytic performances based on normalization. It can be intuitively found that the evolution of photocatalytic activity would give us insights into the

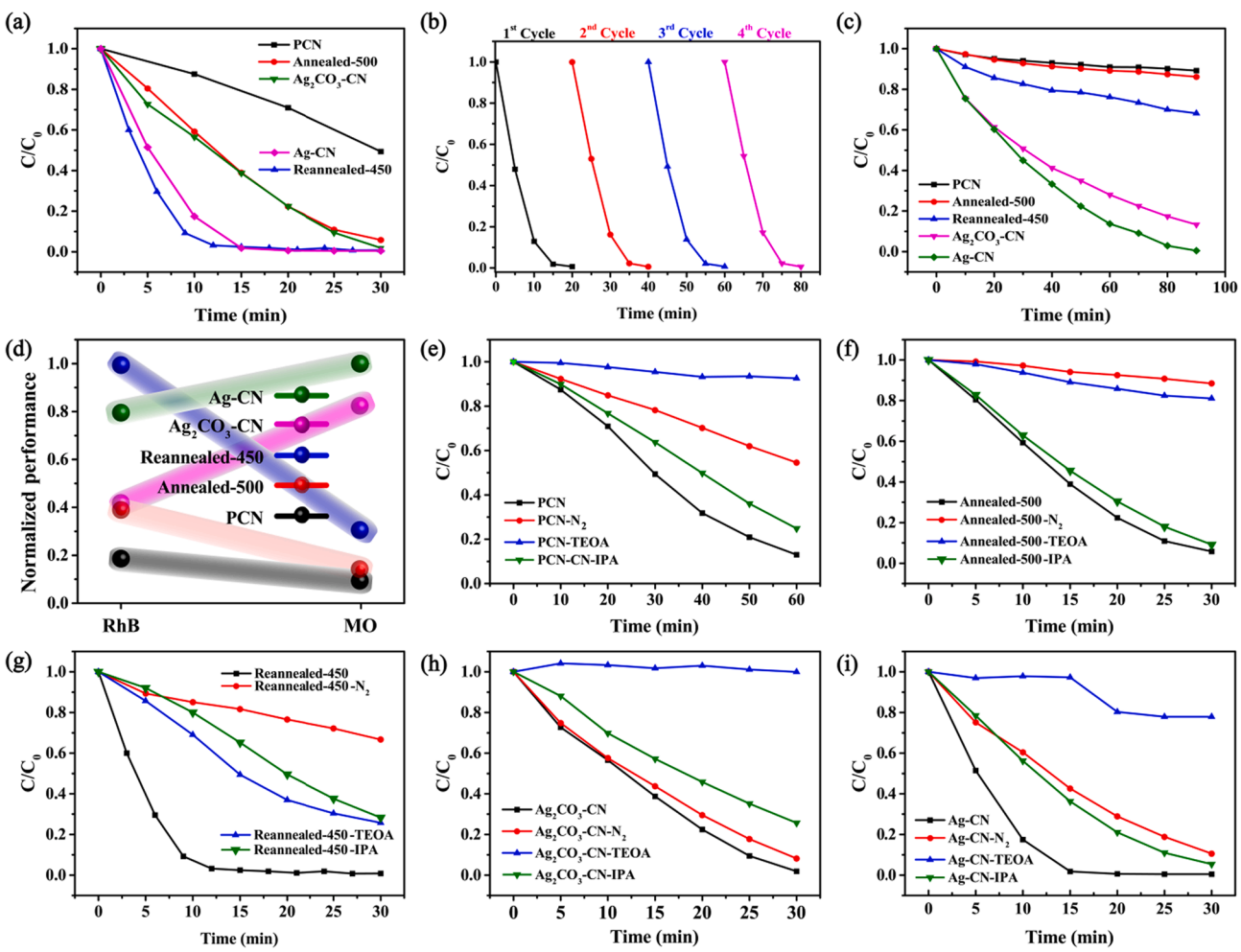

Fig. 6. (a) and (c) Comparison of the photocatalytic activities of PCN-based samples for decomposing the RhB and MO molecules in aqueous solution, respectively. (b) The cyclic test of the RhB molecules degradation over the Ag-CN. (d) Summarized the aforementioned photocatalytic activity of PCN-based samples based on normalization. The effect of a series of scavengers on the decomposition efficiency of the RhB molecules for (e) PCN, (f) Annealed-500, (g) Reannealed-450, (h) Ag_2CO_3-CN and (i) Ag-CN, respectively.

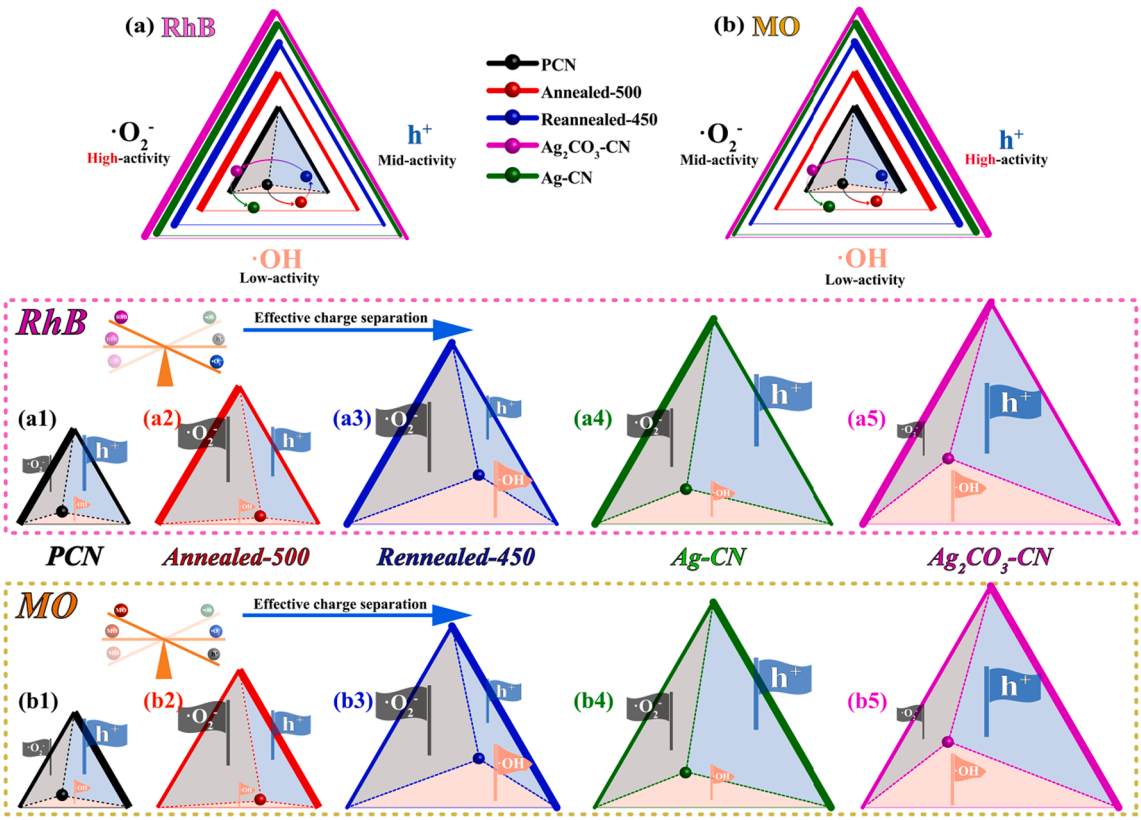

Scheme 2. The illustration of photocatalytic degradation mechanism of active species distribution of PCN-derived samples. The area of each solid line triangles represents the whole amounts of active species (charge separation effect is as inversely proportional to PL intensity, which qualitatively reflects the amount of active species). The area of each divided small triangle (the flags inserted) represents the amount of each active species specifically. Three solid line in each regular triangle corresponds to different active species, and the thickness of the solid line correspond to the ability in decomposing dyes (the thicker, the better), thus, the contribution for decomposing dyes by each active species is not only determined by the area size, but also determined by the thickness of the solid line (weight factor).

relation between active species redistribution and corresponding performance. For example, the higher proportion of the $^{\bullet}O_2^-$ will facilitate the RhB molecules decomposition effectively (Comparing the species trapping experiments of Ag-CN to Ag_2CO_3-CN). The higher proportion of the h^+ can accelerate the MO molecules degradation availably (Comparing the MO degradation activity and species trapping experiments of Annealed-500 to Ag_2CO_3-CN). The phenomenon also can be interpreted as the effect of electrostatic attraction. As RhB molecules and $^{\bullet}O_2^-$ are positively and negatively charged (as well as h^+ and MO molecules) [49], respectively, the effect of electrostatic attraction will facilitate adsorption to enhance the degradation performance. Thus RhB molecules can be efficiently decomposed by $^{\bullet}O_2^-$ and MO molecules can be effectively degraded by h^+, respectively. These results guide us that purposeful modifications can decompose specific pollutants effectively. Take for example, the photocatalyst of reannealed-450 can be used to specialize in decomposing RhB pollutant, and Ag-CN can be selected to degrade mixture pollutant of RhB and MO. Meanwhile, it also indicates that the simple effectively charge separation induced enhancement mechanism is not sufficient to explain all photocatalytic degradation phenomena, which is in agreement with the most published results reported elsewhere [17,18].

3.4. Photocatalytic mechanism analysis

To reveal the mechanism that behind the photocatalytic performance variation of the PCN-composites, the active species contribution was further investigated. The species trapping experiments were carried out in photocatalytic decomposing RhB molecules process. The certain scavengers were added to the reaction system, where N_2 avoiding oxygen to produce superoxide anion radicals ($^{\bullet}O_2^-$), triethanolamine (TEOA, 10%) capturing holes (h^+) and isopropanol (IPA, 10%) scavenging for hydroxyl radicals ($^{\bullet}OH$). It can be obviously found that the dominant active species are totally different (Fig. 6e-i). Specifically, the h^+ and $^{\bullet}O_2^-$ are major active species in the PCN reaction system. The $^{\bullet}O_2^-$ and h^+ are the primary active species in annealed-500 degradation system. The obviously enhanced photocatalytic activity of reannealed-450 is ascribed to the contribution of $^{\bullet}O_2^-$ and $^{\bullet}OH$ active species. Thus it is known that the $^{\bullet}O_2^-$ active species becomes the most crucial contributor after the annealing process, which are also in agreement with Song's report [50]. In fact, the oxygen atom doping in CN nanosheets structure facilitate the formation of $^{\bullet}O_2^-$ because of the excited electrons combining with O_2 more easily. The relatively poor performance of Ag_2CO_3-CN can be ascribed to that the h^+ and $^{\bullet}OH$ active species dominate the degradation system. After converting Ag_2CO_3-CN to Ag-CN, the photocatalytic activity is governed by the active species of h^+ and $^{\bullet}O_2^-$, and thus it performed enhancing degradation activity comparing with Ag_2CO_3-CN (The details of degradation process reflected by the optical absorption spectra can be intuitively found in Fig. S9).

It is widely accepted that the structural modification causes the variation of proportion of generated active species, meaning that each step of structural modification leads to the generation of a high percentage of the specific active species [19–21,51–53]. Furthermore, according to the aforementioned phenomenon that we verified, it can be known that the effectively spatial separation of photo-excited e-h pairs are presumably essential for enhancing the total amount of active species when reaching the dynamic equilibrium [54]. Meanwhile, Guan and co-workers also reported that employing TiO_2 as an example to make an

important contribution to a comprehensive understanding of the charge transport inside the crystal and the preferred accumulation of electrons and holes on the surface [55]. Thus, we propose a photodegradation model illustrated in Scheme 2 according to the decomposition behavior in organic dyes of RhB and MO, which reveals the enhancement mechanism from the viewpoints by combining both effective charge separation and proportion evolution of active species. Degradation of organic pollutants mainly depends on active species (holes, $^{\bullet}O_2^-$, $^{\bullet}OH$), which the whole amounts of active species can be represented by a triangle. The size of this triangle corresponds to the efficiency of charge separation (the bigger, the better). In this triangle, we aim to distinguish the degradation contribution of specific active species according to each divided smaller triangle (the bigger, the higher). Meanwhile, the different organic pollutants can be decomposed by specific active species. For example, it can be verified that the holes (h^+) is effective for MO degradation and superoxide anion radicals ($^{\bullet}O_2^-$) is effective for RhB degradation. It can be based on this feature using the thickness of the three sides of the triangle to represent the relationship between specific pollutants and most suitable active species (the thicker, the better). The routes of moving points in the triangle show the different modified treatment processes step by step, which is insightfully reflected the relationship between structure modified and the photocatalytic activity evolution. In other words, each solid line regular triangle area represents catalytic contributions of the whole active species (inversely proportional to the PL intensity), and the area size of each divided smaller dashed-line triangle (the different flags inserted) in each regular triangles, represents the amount of each specific active species(Scheme 2a1-a5 and 2b1-b5). The routes of moving points in Scheme 2a and b show the different modified treatment processes step by step. Therefore, Scheme 2 can let us directly understand that the overall photocatalytic activity is not only determined by the total amounts of active species produced (efficient charge separation), but also depends on the proportion of each active species. For example, the degradation activity of PCN is much worse than that of Ag-CN shown in Fig. 6d though they possess the same active species rankings (Fig. 6e and i). The enhanced photocatalytic activity of Ag-CN probably attributed to sufficient active species amounts as reflected by Scheme a1 and a4 (decreased PL intensity corresponds to effective charge separation). The enhanced photocatalytic activity of both annealed samples (red and blue points) compared to the PCN (black point) is mainly attributed to increased whole amounts of radicals (reflected by PL curves in Fig. 5e) and the higher proportion of the $\bullet O_2^-$ active species (Scheme a1, a2 and a3). Ag_2CO_3-CN (pink point) and Ag-CN (green point) possibly possess similar amounts of active species (reflected by PL curves in Fig. 5f). As h^+ is the most efficient active species to degrade the MO molecules, and both heterojunction samples have the highest proportion of h^+ among active species (comparing area size of blue triangles in Scheme b4 and b5), as a consequence, the activity of Ag_2CO_3-CN and Ag-CN in degradation of MO does not show obvious difference (90 min, 85% vs 95%, respectively). On the other hand, as $\bullet O_2^-$ is the most effective active species for decomposing RhB, Ag-CN (12 min, 95%) shows much better performance in degradation of RhB than that of Ag_2CO_3-CN (30 min, 95%) due to the different proportion of $^{\bullet}O_2^-$ (comparing area size of grey triangles in Scheme a4 and a5. Moreover, the relationship between evolution of PL intensity and difference of photocatalytic activity also can be insightful realized. The PL intensity shows that photo-excited carriers recombination is suppressed after annealing treatment. According to our group previous works [23], for PCN, photo-excited carriers in energy space are not effectively separated in real space, and it can be reflected by the prominent PL intensity, indicating that the recombination portion of photo-excited electron-hole pairs is relatively high. On the contrary, any accessible atomic oxygenation sites may cause the breaking of uniformly distributed density of charge states in real space for both valance band and conduction band. Therefore, the recombination of photo-excited carriers of annealed samples is effectively hindered in both energy space and real space, and obviously enhancing the photocatalytic activity due to the effectively separated electron-hole pairs. Nevertheless, for Ag_2CO_3-CN and Ag-CN, although they perform lower light excited electrons and holes recombination, the charge effectively separation mechanism is not sufficient to interpret the difference of decomposition behavior for RhB and MO. If we additionally take account of the significance of the active species distribution, the phenomenon can be reasonably explained. Here, based on the above discussion, for each active species, the photocatalytic activity for decomposing different dyes is illustrated in Scheme S1. Therefore, we firmly believe that this work not only presents a facile route to enhance photocatalytic performance of PCN-based materials, but the more important is that it reveals the enhancement mechanism from the combined viewpoints of effective charge separation and the significance of redistributed proportion evolution of active species.

4. Conclusions

In summary, we propose a mechanism that gives insights into what is happening to organic pollutants degradation behavior. Based on this, we successfully designed a 4-step route to synthesize a PCN-based photocatalyst (Ag-CN) with extremely high efficiency in degradation of various pollutant dyes. The essence of CN structural modification induced photocatalytic activity variation (i.e. various dyes degradation) is not only determined by the photo-excited e-h pair separation, but also dominated by the redistribution of active species proportion. The annealing treatment allows the PCN to obtain remarkable large surface and pore volume, introduced oxygen element probably forming active sites to enhance the photocatalytic activity. We show the apparent evidence that though the incorporation of Ag_2CO_3 obviously improves the performance of MO molecules degradation, it is actually at the expense of the RhB degradation activity. Namely, it also can be interpreted as the process of active species redistribution to increase the proportion of radicals that facilitate the MO molecules decomposition, and the corresponding proportion of active species that decelerates the RhB molecules degradation. Furthermore, the holes (h^+) and superoxide anion radicals ($^{\bullet}O_2^-$) were further verified that are most effective for the MO and RhB molecules degradation, respectively. Thus, the mechanism is of great significance for purposefully conducting further investigation of more and more potential behavior of PCN-based degradation, and even applied to other materials.

Funding sources

The work is supported by the National Science Foundation of China for Distinguished Young Scholars (Grant No. 61525404), CAS Pioneer Hundred Talents Program, and the National Natural Science Foundation of China (Grant No. 51773171).

Declaration of Competing Interest

The authors declare no competing financial interest.

Acknowledgements

The authors acknowledge Mr. Jinming Wang for TEM test, Dr. Yun Yang for AFM test, Mr. Bo Chen for BET test, Mr. Yange Wang for UV-Vis DRS measurement, Dr. Qingchi Xu for PL test and Mr. Zhaohui Meng for SEM test, respectively.

Appendix A. Supplementary material

Supplementary data to this article can be found online at https://doi.org/10.1016/j.apsusc.2021.149099.

References

[1] S. Xiao, D. Zhang, D. Pan, W. Zhu, P. Liu, Y. Cai, G. Li, H. Li, A chloroplast structured photocatalyst enabled by microwave synthesis, Nat. Commun. 10 (2019) 1570.

[2] R. Zhang, Z. Huang, C. Li, Y. Zuo, Y. Zhou, Monolithic g-C_3N_4/reduced graphene oxide aerogel with in situ embedding of Pd nanoparticles for hydrogenation of CO_2 to CH_4, Appl. Surf. Sci. 475 (2019) 953–960.

[3] A. Fujishima, K. Honda, Electrochemical Photolysis of Water at a Semiconductor Electrode, Nature 238 (1972) 37–38.

[4] X. Lan, T. Wang, Highly Selective Catalysts for the Hydrogenation of Unsaturated Aldehydes: A Review, ACS Catal. 10 (2020) 2764–2790.

[5] N. Mao, J.-X. Jiang, MgO/g-C_3N_4 nanocomposites as efficient water splitting photocatalysts under visible light irradiation, Appl. Surf. Sci. 476 (2019) 144–150.

[6] S. Xiao, W. Dai, X. Liu, D. Pan, H. Zou, G. Li, G. Zhang, C. Su, D. Zhang, W. Chen, H. Li, Microwave-Induced Metal Dissolution Synthesis of Core-Shell Copper Nanowires/ZnS for Visible Light Photocatalytic H_2 Evolution, Adv. Energy Mater. 9 (2019).

[7] K. Maeda, M. Higashi, D. Lu, R. Abe, K. Domen, Efficient Nonsacrificial Water Splitting through Two-Step Photoexcitation by Visible Light using a Modified Oxynitride as a Hydrogen Evolution Photocatalyst, J. Am. Chem. Soc. 132 (2010) 5858–5868.

[8] A. Kudo, Y. Miseki, Heterogeneous photocatalyst materials for water splitting, Chem. Soc. Rev. 38 (2009) 253–278.

[9] X. Wang, K. Maeda, A. Thomas, K. Takanabe, G. Xin, J.M. Carlsson, K. Domen, M. Antonietti, A metal-free polymeric photocatalyst for hydrogen production from water under visible light, Nat. Mater. 8 (2009) 76–80.

[10] J. Fu, J. Yu, C. Jiang, B. Cheng, g-C_3N_4-Based Heterostructured Photocatalysts, Adv. Energy Mater. 8 (2018) 1701503.

[11] Q. Li, N. Zhang, Y. Yang, G. Wang, D.H. Ng, High efficiency photocatalysis for pollutant degradation with MoS_2/C_3N_4 heterostructures, Langmuir 30 (2014) 8965–8972.

[12] M. Zhou, Z. Hou, X. Chen, Graphitic-C_3N_4 nanosheets: synergistic effects of hydrogenation and n/n junctions for enhanced photocatalytic activities, Dalton Trans. 46 (2017) 10641–10649.

[13] M. Zhou, Z. Hou, X. Chen, The Effects of Hydrogenation on Graphitic C_3N_4 Nanosheets for Enhanced Photocatalytic Activity, Part Part Syst Charact 35 (2018) 1700038.

[14] M. Zhou, Z. Hou, L. Zhang, Y. Liu, Q. Gao, X. Chen, n/n junctioned g-C_3N_4 for enhanced photocatalytic H_2 generation, Sustain. Energy Fuels 1 (2017) 317–323.

[15] J.-H. Wu, F.-Q. Shao, X.-Q. Luo, H.-J. Xu, A.-J. Wang, Pd nanocones supported on g-C_3N_4: An efficient photocatalyst for boosting catalytic reduction of hexavalent chromium under visible-light irradiation, Appl. Surf. Sci. 471 (2019) 935–942.

[16] M. Wang, G. Tan, H. Ren, A. Xia, Y. Liu, Direct double Z-scheme O-g-C_3N_4/Zn_2SnO_4N/ZnO ternary heterojunction photocatalyst with enhanced visible photocatalytic activity, Appl. Surf. Sci. 492 (2019) 690–702.

[17] J. Low, C. Jiang, B. Cheng, S. Wageh, A.A. Al-Ghamdi, J. Yu, A Review of Direct Z-Scheme Photocatalysts, Small Methods 1 (2017) 1700080.

[18] Q. Xu, L. Zhang, B. Cheng, J. Fan, J. Yu, S-Scheme Heterojunction Photocatalyst, Chem 6 (2020) 1543–1559.

[19] J. Feng, D. Zhang, H. Zhou, M. Pi, X. Wang, S. Chen, Coupling P Nanostructures with P-Doped g-C_3N_4 As Efficient Visible Light Photocatalysts for H_2 Evolution and RhB Degradation, ACS Sustain. Chem. Eng. 6 (2018) 6342–6349.

[20] G. Tan, L. She, T. Liu, C. Xu, H. Ren, A. Xia, Ultrasonic chemical synthesis of hybrid mpg-C_3N_4/$BiPO_4$ heterostructured photocatalysts with improved visible light photocatalytic activity, Appl. Catal. B 207 (2017) 120–133.

[21] Y. Jiang, P. Liu, Y. Chen, Z. Zhou, H. Yang, Y. Hong, F. Li, L. Ni, Y. Yan, D. H. Gregory, Construction of stable Ta_3N_5/g-C_3N_4 metal/non-metal nitride hybrids with enhanced visible-light photocatalysis, Appl. Surf. Sci. 391 (2017) 392–403.

[22] A. Shi, H. Li, S. Yin, J. Zhang, Y. Wang, H_2 Evolution over g-C_3N_4/Cs_xWO_3 under NIR light, Appl. Catal. B 228 (2018) 75–86.

[23] Y. Gong, H. Li, C. Jiao, Q. Xu, X. Xu, X. Zhang, Y. Liu, Z. Dai, X.Y. Liu, W. Chen, L. Liu, D. Zhan, Effective hydrogenation of g-C_3N_4 for enhanced photocatalytic performance revealed by molecular structure dynamics, Appl. Catal. B 250 (2019) 63–70.

[24] J. Xiao, Q. Han, H. Cao, J. Rabeah, J. Yang, Z. Guo, L. Zhou, Y. Xie, A. Brückner, Number of Reactive Charge Carriers-A Hidden Linker between Band Structure and Catalytic Performance in Photocatalysts, ACS Catal. 9 (2019) 8852–8861.

[25] Z. Zhang, C. Liu, Z. Dong, Y. Dai, G. Xiong, Y. Liu, Y. Wang, Y. Wang, Y. Liu, Synthesis of flower-like MoS_2/g-C_3N_4 nanosheet heterojunctions with enhanced photocatalytic reduction activity of uranium(VI), Appl. Surf. Sci. 520 (2020), 146352.

[26] Y. Yuan, L. Zhang, J. Xing, M.I. Utama, X. Lu, K. Du, Y. Li, X. Hu, S. Wang, A. Genc, R. Dunin-Borkowski, J. Arbiol, Q. Xiong, High-yield synthesis and optical properties of g-C_3N_4, Nanoscale 7 (2015) 12343–12350.

[27] R. Bhosale, S. Jain, C.P. Vinod, S. Kumar, S. Ogale, Direct Z-Scheme g-C_3N_4/$FeWO_4$ Nanocomposite for Enhanced and Selective Photocatalytic CO_2 Reduction under Visible Light, ACS Appl. Mater. Interfaces 11 (2019) 6174–6183.

[28] G. Zhang, G. Li, Z.A. Lan, L. Lin, A. Savateev, T. Heil, S. Zafeiratos, X. Wang, M. Antonietti, Optimizing Optical Absorption, Exciton Dissociation, and Charge Transfer of a Polymeric Carbon Nitride with Ultrahigh Solar Hydrogen Production Activity, Angew. Chem. Int. Ed. 56 (2017) 13445–13449.

[29] L.-X. Su, Q. Lou, C.-X. Shan, D.-L. Chen, J.-H. Zang, L.-J. Liu, Ag/Nanodiamond/g-C_3N_4 heterostructures with enhanced visible-light photocatalytic performance, Appl. Surf. Sci. 525 (2020), 146576.

[30] M. Chen, C. Guo, S. Hou, L. Wu, J. Lv, C. Hu, Y. Zhang, J. Xu, In-situ fabrication of Ag/P-g-C_3N_4 composites with enhanced photocatalytic activity for sulfamethoxazole degradation, J. Hazard. Mater. 366 (2019) 219–228.

[31] P. Niu, L. Zhang, G. Liu, H.-M. Cheng, Graphene-Like Carbon Nitride Nanosheets for Improved Photocatalytic Activities, Adv. Funct. Mater. 22 (2012) 4763–4770.

[32] C. Liu, H. Huang, W. Cui, F. Dong, Y. Zhang, Band structure engineering and efficient charge transport in oxygen substituted g-C_3N_4 for superior photocatalytic hydrogen evolution, Appl. Catal. B 230 (2018) 115–124.

[33] H. Wang, Y. Su, H. Zhao, H. Yu, S. Chen, Y. Zhang, X. Quan, Photocatalytic oxidation of aqueous ammonia using atomic single layer graphitic-C_3N_4, Environ. Sci. Technol. 48 (2014) 11984–11990.

[34] Z. Mo, H. Xu, Z. Chen, X. She, Y. Song, J. Lian, X. Zhu, P. Yan, Y. Lei, S. Yuan, H. Li, Construction of MnO_2/Monolayer g-C_3N_4 with Mn vacancies for Z-scheme overall water splitting, Appl. Catal. B 241 (2019) 452–460.

[35] Q. Liu, J. Shen, X. Yu, X. Yang, W. Liu, J. Yang, H. Tang, H. Xu, H. Li, Y. Li, J. Xu, Unveiling the origin of boosted photocatalytic hydrogen evolution in simultaneously (S, P, O)-Codoped and exfoliated ultrathin g-C_3N_4 nanosheets, Appl. Catal. B 248 (2019) 84–94.

[36] J. Zhang, J. Chen, Y. Wan, H. Liu, W. Chen, G. Wang, R. Wang, Defect Engineering in Atomic-Layered Graphitic Carbon Nitride for Greatly Extended Visible-Light Photocatalytic Hydrogen Evolution, ACS Appl. Mater. Interfaces 12 (2020) 13805–13812.

[37] J. Barrio, L. Lin, X. Wang, M. Shalom, Design of a Unique Energy-Band Structure and Morphology in a Carbon Nitride Photocatalyst for Improved Charge Separation and Hydrogen Production, ACS Sustain. Chem. Eng. 6 (2017) 519–530.

[38] L. Ming, H. Yue, L. Xu, F. Chen, Hydrothermal synthesis of oxidized g-C_3N_4 and its regulation of photocatalytic activity, J. Mater. Chem. A 2 (2014) 19145–19149.

[39] S. Hua, D. Qu, L. An, W. Jiang, Y. Wen, X. Wang, Z. Sun, Highly efficient p-type Cu_3P/n-type g-C_3N_4 photocatalyst through Z-scheme charge transfer route, Appl. Catal. B 240 (2019) 253–261.

[40] J. Li, B. Shen, Z. Hong, B. Lin, B. Gao, Y. Chen, A facile approach to synthesize novel oxygen-doped g-C_3N_4 with superior visible-light photoreactivity, Chem. Commun. 48 (2012) 12017–12019.

[41] Y. Li, L. Fang, R. Jin, Y. Yang, X. Fang, Y. Xing, S. Song, Preparation and enhanced visible light photocatalytic activity of novel g-C_3N_4 nanosheets loaded with Ag_2CO_3 nanoparticles, Nanoscale 7 (2015) 758–764.

[42] H. Tang, S. Chang, G. Tang, W. Liang, AgBr and g-C_3N_4 co-modified Ag_2CO_3 photocatalyst: A novel multi-heterostructured photocatalyst with enhanced photocatalytic activity, Appl. Surf. Sci. 391 (2017) 440–448.

[43] A. Mirzaei, Z. Chen, F. Haghighat, L. Yerushalmi, Magnetic fluorinated mesoporous g-C_3N_4 for photocatalytic degradation of amoxicillin: Transformation mechanism and toxicity assessment, Appl. Catal. B 242 (2019) 337–348.

[44] J. Yuan, X. Yi, Y. Tang, C. Liu, S. Luo, Efficient Photocatalytic Hydrogen Evolution and CO_2 Reduction: Enhanced Light Absorption, Charge Separation, and Hydrophilicity by Tailoring Terminal and Linker Units in g-C_3N_4, ACS Appl. Mater. Interfaces 12 (2020) 19607–19615.

[45] W. Wang, J. Fang, X. Huang, Different behaviors between interband and intraband transitions generated hot carriers on g-C_3N_4/Au for photocatalytic H_2 production, Appl. Surf. Sci. 513 (2020), 145830.

[46] X. Hu, X. Zeng, Y. Liu, J. Lu, S. Yuan, Y. Yin, J. Hu, D.T. McCarthy, X. Zhang, Nano-layer based 1T-rich MoS_2/g-C_3N_4 co-catalyst system for enhanced photocatalytic and photoelectrochemical activity, Appl. Catal. B 268 (2020).

[47] F. Shao, L. Mi, Z. Tian, C. Zheng, Y. Zhang, Q. Li, S. Liu, Promoting Photodegradation Efficiency via a Heterojunction Photocatalyst Combining with Oxygen Direct and Fast Diffusion from the Gas Phase to Active Catalytic Sites, ACS Appl. Mater. Interfaces 11 (2019) 44922–44930.

[48] M. Green, Z. Liu, R. Smedley, H. Nawaz, X. Li, F. Huang, X. Chen, Graphitic carbon nitride nanosheets for microwave absorption, Mater. Today Phys. 5 (2018) 78–86.

[49] X. Xie, X. Huang, W. Lin, Y. Chen, X. Lang, Y. Wang, L. Gao, H. Zhu, J. Chen, Selective Adsorption of Cationic Dyes for Stable Metal-Organic Framework ZJU-48, ACS Omega 5 (2020) 13595–13600.

[50] Y. Song, X. She, J. Yi, Z. Mo, L. Liu, H. Xu, H. Li, Single layer two-dimensional O-g-C3N4: An efficient photocatalyst for improved molecular oxygen activation ability, Phys. Status Solidi (a), 214 (2017) 1600704.

[51] J. Zhang, Y. Hu, X. Jiang, S. Chen, S. Meng, X. Fu, Design of a direct Z-scheme photocatalyst: preparation and characterization of Bi_2O_3/g-C_3N_4 with high visible light activity, J. Hazard. Mater. 280 (2014) 713–722.

[52] Y. Hong, Y. Jiang, C. Li, W. Fan, X. Yan, M. Yan, W. Shi, In-situ synthesis of direct solid-state Z-scheme V_2O_5/g-C_3N_4 heterojunctions with enhanced visible light efficiency in photocatalytic degradation of pollutants, Appl. Catal. B 180 (2016) 663–673.

[53] X. Xiao, J. Wei, Y. Yang, R. Xiong, C. Pan, J. Shi, Photoreactivity and Mechanism of g-C_3N_4 and Ag Co-Modified Bi_2WO_6 Microsphere under Visible Light Irradiation, ACS Sustain. Chem. Eng. 4 (2016) 3017–3023.

[54] F. Yi, H. Gan, H. Jin, W. Zhao, K. Zhang, H. Jin, H. Zhang, Y. Qian, J. Ma, Sulfur- and chlorine-co-doped g-C_3N_4 nanosheets with enhanced active species generation for boosting visible-light photodegradation activity, Sep. Purif. Technol. 233 (2020), 115997.

[55] L. Guan, X. Chen, The photoexcited charge transport and accumulation in anatase TiO_2, ACS Appl. Energy Mater. 1 (2018) 4313–4320.